Journal of Applied Mechanics and Technical Physics, Vol. 49, No. 5, pp. 789–798, 2008

FLOW OF A DISPERSED PHASE IN THE LAVAL NOZZLE AND IN THE TEST SECTION OF A TWO-PHASE HYPERSONIC SHOCK TUNNEL

A. A. Verevkin and Yu. M. Tsirkunov

UDC 532.529.5:533.7

An unsteady gas–particle flow in a hypersonic shock tunnel is studied numerically. The study is performed in the period from the instant when the diaphragm between the high-pressure and low-pressure chambers is opened until the end of the transition to a quasi-steady flow in the test section. The dispersed phase concentration is extremely low, and the collisions between the particles and their effect on the carrier gas flow are ignored. The particle size is varied. The time evolution of the particle concentration in the test section is obtained. Patterns of the quasi-steady flow of the dispersed phase in the throat of the Laval nozzle and the flow around a model (sphere) are presented. Particle concentration and particle velocity lag profiles at the test-section entrance are obtained. The particle-phase flow structure and the time needed for it to reach a quasi-steady regime are found to depend substantially on the particle size.

Key words: *shock tunnel, Laval nozzle, two-phase gas–particle flow, flow around a body, numerical simulations.*

Introduction. Shock tunnels have been used for experimental research of aerodynamics and physical gasdynamics problems for more than half a century [1]. Comparatively recently, such shock tunnels have been used to study hypersonic dusty-gas flows. The results of research performed in a UT-1M experimental setup at the Central Hydroaerodynamic Institute (TsAGI) are the most well-known ones. A hypersonic two-phase shock tunnel is a classical shock tunnel with an attached hypersonic contoured nozzle generating a high-velocity flow in the test section connected at the end with a vacuum chamber. For a two-phase flow to be produced in the test section, dispersed particles are injected into the high-pressure chamber at the instant of wind-tunnel start-up; these particles are then entrained by the gas flow. The structure of the unsteady gas flow developing in such a shock tunnel after diaphragm opening was studied in detail in [3]. First, a strong shock wave is formed, which moves toward the nozzle. When this wave is reflected from the nozzle walls, transverse shock waves are formed. These waves interact with each other and with the nozzle walls both regularly and irregularly with formation of triple (Mach) configurations. As a result, two intense near-axis vortices come into being and develop in the nozzle throat; later on, these vortices are entrained downstream. At the initial stage, however, these vortices exert a significant effect on the behavior of the particle phase, in particular, on the motion of fine particles. Because of different inertial properties, fine and coarse particles behave differently in an unsteady flow in the nozzle and test section. Coarse particles lag behind the carrier gas, collide with the walls of the converging part of the Laval nozzle, and are reflected from the walls. This results in redistribution of particles in the transverse direction, and the two-phase flow in the test section may become substantially nonuniform. Moreover, because of the lag of the particles from the carrier gas (lower velocity of particles, as compared with the gas velocity) and complicated interaction of the front of the cloud of particles with the model in the test section, the beginning of the quasi-steady two-phase flow is delayed with respect to the pure gas flow around the model.

Ustinov Voenmekh Baltic State Technical University, St. Petersburg 190005; tsrknv@bstu.spb.su. Translated from Prikladnaya Mekhanika i Tekhnicheskaya Fizika, Vol. 49, No. 5, pp. 102–113, September–October, 2008. Original article submitted April 5, 2007; revision submitted June 25, 2007.

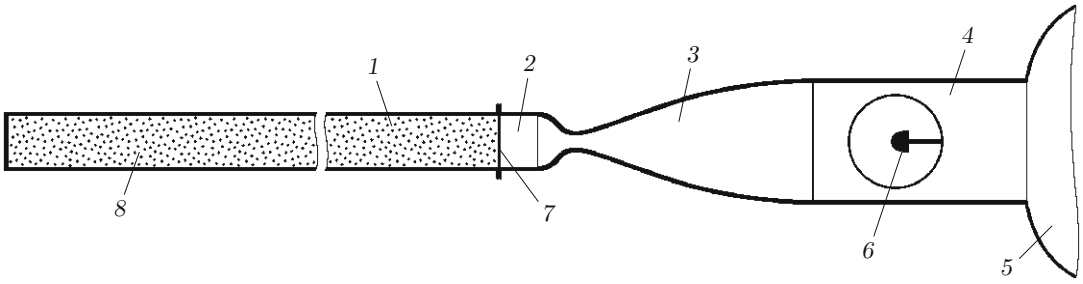

Fig. 1. Schematic of a hypersonic shock tunnel: 1) high-pressure chamber; 2) low-pressure chamber; 3) Laval nozzle; 4) test section; 5) vacuum chamber; 6) model; 7) diaphragm; 8) particles.

The goal of this work is a numerical simulation of the transition of an essentially unsteady initial two-phase flow to a quasi-steady regime and of the structure of the particle-phase flow in the nozzle and test section near the immersed model in this regime. The results of the study may significantly affect the choice of the model position in the test section in a real experiment and interpretation of measurement results in an extremely short-time quasi-steady flow regime.

Schematic Layout of a Hypersonic Shock Tunnel and Initial Parameters. Numerical simulations were performed for a flow in a shock tunnel and a nozzle with configurations similar to the UT-1M setup at TsAGI. The layout of this setup is shown in Fig. 1. The shock tunnel is assumed to be a cylinder with the diameter equal to the diameter of the nozzle-entrance cross section; the length of the high-pressure chamber is 6 m. The design Mach number at the exit of an axisymmetric contoured nozzle is $\mathrm{M}_a = 6.01$, the diameters of the nozzle-entrance, throat, and nozzle-exit cross sections are 76, 38, and 277.4 mm, respectively, the nozzle length is 1.6 m, and the distance between the diaphragm and the throat is 0.4 m. The test-section diameter is assumed to be equal to the nozzle-exit diameter. The model (sphere) is placed in the test section. The initial parameters of the gas (air) are the same as those in physical experiments: the pressure and temperature in the high-pressure chamber are 25 atm and 600 K (the air is heated to avoid its condensation during expansion in the Laval nozzle); the pressures and temperatures in the low-pressure chamber, nozzle, and vacuum chamber are 0.01 atm and 290 K. The model 20 mm in diameter is located at a distance of 250 mm from the nozzle exit. The dispersed particles are assumed in simulations to be uniformly distributed over the entire high-pressure chamber at the instant of shock-tunnel start-up (diaphragm opening). The initial volume fraction of particles is assumed to be $\alpha_{p\infty} = 10^{-7}$. The particles are assumed to have a spherical shape, and the particle material is silicon dioxide (with a density $\rho_p = 2264\ \mathrm{kg/m^3}$). The particle diameter d_p is varied from 0.15 to 40 μm. Particles of the smallest diameter flew around the model without collisions with the model surface.

Mathematical Model of a Two-Phase Flow. Theoretical estimates obtained on the basis of the approach [4] and simulation results [3] show that, for the initial volume fraction of particles in the high-pressure chamber $\alpha_{p\infty} < 10^{-6}$, the effect of the particle phase on the carrier gas flow in the entire flow region and the collisions of incident and reflected particles in the flow around a blunt body in the test section are not important and can be neglected. In this case, simulation of a two-phase flow reduces to consecutive solution of two problems: calculating the carrier gas flow with no allowance for the influence of the dispersed phase and determining the particle motion in a known unsteady gas flow field.

The flow region includes the high-pressure and low-pressure chambers, the nozzle, and the test section. The flow of each phase is assumed to be axisymmetric. The computational domain in the plane (x, y) is bounded by the channel walls, body surface, axis of symmetry, and exit plane of the test section.

The motion of the carrier medium is described by the Euler equations for a perfect gas, which are written in the following form in a cylindrical coordinate system (the x axis is directed along the axis of symmetry and the y axis is perpendicular to the x axis):

$$\frac{\partial \boldsymbol{U}}{\partial t} + \frac{\partial \boldsymbol{F}}{\partial x} + \frac{\partial \boldsymbol{G}}{\partial y} + \frac{\boldsymbol{H}}{y} = 0. \tag{1}$$

Here

$$\boldsymbol{U} = \begin{pmatrix} \rho \\ \rho u \\ \rho v \\ \rho e \end{pmatrix}, \quad \boldsymbol{F} = \begin{pmatrix} \rho u \\ \rho u^2 + p \\ \rho uv \\ (\rho e + p)u \end{pmatrix}, \quad \boldsymbol{G} = \begin{pmatrix} \rho v \\ \rho uv \\ \rho v^2 + p \\ (\rho e + p)v \end{pmatrix}, \quad \boldsymbol{H} = \begin{pmatrix} \rho v \\ \rho uv \\ \rho v^2 \\ (\rho e + p)v \end{pmatrix},$$

$$e = c_v T + (u^2 + v^2)/2, \qquad p = \rho RT.$$

The boundary conditions are formulated as follows. The conditions of zero normal velocity $\boldsymbol{v} \cdot \boldsymbol{n}_w = 0$ ($\boldsymbol{n}_w$ is the unit normal to the wetted surface directed inward the channel) are set on all channel walls and on the model surface; the conditions of symmetry $v = \partial\rho/\partial y = \partial T/\partial y = \partial u/\partial y = 0$ are imposed on the axis $y = 0$. The so-called "soft" boundary conditions are set at the exit from the test section to the vacuum chamber, where the flow is supersonic (in the numerical algorithm, the flow parameters are shifted to the exit boundary from the near-boundary cells).

The initial pressure and temperature in the high-pressure and low-pressure chambers, Laval nozzle, and test section are defined, as indicated above. The density is calculated from the equations of state. The gas velocity equal zero everywhere.

Because of an extremely low particle concentration, the particle-phase flow is realized in the so-called regime of single particles. The model of the force action on the particle includes the aerodynamic drag force $\boldsymbol{f}_D$ induced by the difference in phase velocities, the transverse Magnus force $\boldsymbol{f}_{\mathrm{M}}$, which is significant for reflected particles twisted during their impact on the surface, and the damping torque $\boldsymbol{l}_p$ acting on a rotating particle. Other components of interphase interaction and the gravity force are inessential for this problem. The equations of particle dynamics supplemented by the kinematic relation for trajectory simulations have the form

$$m_p \frac{d\boldsymbol{v}_p}{dt} = \boldsymbol{f}_D + \boldsymbol{f}_{\mathrm{M}}, \qquad J_p \frac{d\boldsymbol{\omega}_p}{dt} = \boldsymbol{l}_p, \qquad \frac{d\boldsymbol{r}_p}{dt} = \boldsymbol{v}_p, \tag{2}$$

where m_p and J_p are the particle mass and moment of inertia; $\boldsymbol{\omega}_p$ and $\boldsymbol{l}_p$ are the angular velocity of the particle and the damping torque acting on a rotating particle from the gas. In an axisymmetric flow, the vectors $\boldsymbol{\omega}_p$ and $\boldsymbol{l}_p$ have nonzero components only in the direction perpendicular to the plane (x, y). The expressions for $\boldsymbol{f}_D$, $\boldsymbol{f}_{\mathrm{M}}$, and $\boldsymbol{l}_p$ are usually presented in the form

$$\boldsymbol{f}_D = (1/2)C_D \pi r_p^2 \rho |\boldsymbol{v} - \boldsymbol{v}_p|(\boldsymbol{v} - \boldsymbol{v}_p); \tag{3}$$

$$\boldsymbol{f}_{\mathrm{M}} = (4/3)C_\omega \pi r_p^3 \rho[(\boldsymbol{\omega} - \boldsymbol{\omega}_p) \times (\boldsymbol{v} - \boldsymbol{v}_p)], \qquad \boldsymbol{\omega} = (1/2)\,\mathrm{rot}\,\boldsymbol{v}; \tag{4}$$

$$\boldsymbol{l}_p = (1/2)C_l r_p^5 \rho |\boldsymbol{\omega} - \boldsymbol{\omega}_p|(\boldsymbol{\omega} - \boldsymbol{\omega}_p). \tag{5}$$

The drag coefficient C_D in Eq. (3) is calculated on the basis of the approximating relations [5]

$$C_D = \begin{cases} C_D^1, & 0 \leqslant \mathrm{M}_p \leqslant 1, \\ C_{D1}^1 + (4/3)(\mathrm{M}_p - 1)(C_{D2}^2 - C_{D1}^1), & 1 < \mathrm{M}_p \leqslant 1.75, \\ C_D^2, & \mathrm{M}_p > 1.75, \end{cases}$$

$$C_D^1\Big(\mathrm{Re}_p, \mathrm{M}_p, \frac{T_p}{T}\Big) = 24\Big\{\mathrm{Re}_p + \mathrm{M}_p\sqrt{\frac{\gamma}{2}}\,\Big[4.33 + \frac{3.65 - 1.53T_p/T}{1 + 0.353T_p/T}\exp\Big(-0.247\,\frac{\mathrm{Re}_p}{\mathrm{M}_p}\sqrt{\frac{2}{\gamma}}\Big)\Big]\Big\}^{-1}$$
$$+ \Big(\frac{4.5 + 0.38(0.03\,\mathrm{Re}_p + 0.48\sqrt{\mathrm{Re}_p})}{1 + 0.03\,\mathrm{Re}_p + 0.48\sqrt{\mathrm{Re}_p}} + 0.1\mathrm{M}_p^2 + 0.2\mathrm{M}_p^8\Big)\exp\Big(-\frac{\mathrm{M}_p}{2\sqrt{\mathrm{Re}_p}}\Big) + 0.6\mathrm{M}_p\sqrt{\frac{\gamma}{2}}\,\Big[1 - \exp\Big(-\frac{\mathrm{M}_p}{\mathrm{Re}_p}\Big)\Big], \tag{6}$$

$$C_D^2\Big(\mathrm{Re}_p, \mathrm{M}_p, \frac{T_p}{T}\Big) = \Big[0.9 + \frac{0.34}{\mathrm{M}_p^2} + 1.86\sqrt{\frac{\mathrm{M}_p}{\mathrm{Re}_p}}\,\Big(2 + \frac{4}{\gamma\mathrm{M}_p^2} + \frac{1.058}{\mathrm{M}_p}\sqrt{\frac{2}{\gamma}}\,\sqrt{\frac{T_p}{T}} - \frac{4}{\gamma^2\mathrm{M}_p^4}\Big)\Big]\Big(1 + 1.86\sqrt{\frac{\mathrm{M}_p}{\mathrm{Re}_p}}\Big)^{-1}.$$

Here $\mathrm{M}_p = |\boldsymbol{v} - \boldsymbol{v}_p|/\sqrt{\gamma RT}$ and $\mathrm{Re}_p = \rho|\boldsymbol{v} - \boldsymbol{v}_p|d_p/\mu$ are the particle Mach and Reynolds numbers during the relative motion of the phases, C_{D1}^1 is the value of C_D^1 for $\mathrm{M}_p = 1$, and C_{D2}^2 is the value of C_D^2 for $\mathrm{M}_p = 1.75$.

TABLE 1

Re_ω	C_{l1}	C_{l2}
0–6	0	16π
6–20	5.32	37.20
20–50	6.44	32.20
50–$(4 \cdot 10^4)$	6.45	32.10

The ratio of the particle and carrier gas temperatures T_p/T has a weak effect on the drag coefficient of the particle in a continuum flow [6]. In the present simulations, the influence of the difference in phase temperatures on C_D is ignored, and the ratio T_p/T in Eqs. (6) is assumed to be equal to unity.

To determine the coefficient C_ω in Eq. (4), we use the relations from [7, 8]:

$$C_\omega = \begin{cases} 3[0.45 + (2\zeta - 0.45)\exp(-0.075\zeta^{0.4}\,\mathrm{Re}_\omega^{0.7})]/(8\zeta), & 2\zeta \geqslant 0.45, \\ 3/4, & 2\zeta < 0.45. \end{cases}$$

Here $\zeta = |\boldsymbol{\omega} - \boldsymbol{\omega}_p| r_p / |\boldsymbol{v} - \boldsymbol{v}_p|$.

The coefficient C_l in Eq. (5) is determined by the formula [9]

$$C_l = C_{l1}/\sqrt{\mathrm{Re}_\omega} + C_{l2}/\,\mathrm{Re}_\omega\,.$$

The values of the constants C_{l1} and C_{l2} for various ranges of Re_ω are summarized in Table 1.

The coefficients C_ω and C_l in Eqs. (4) and (5) depend on the rotational particle Reynolds number defined as

$$\mathrm{Re}_\omega = \rho |\boldsymbol{\omega} - \boldsymbol{\omega}_p| r_p^2 / \mu.$$

Conditions for particles on the boundaries of the computational domain depend on the type of the boundary. For particles crossing the axis of symmetry, specular reflection of particles from the axis is assumed. Particles crossing the exit boundary (exit plane of the test section) are eliminated from further consideration. If the particle collides with the walls of the shock-tunnel channel, nozzle, test section, or model, it is assumed to rebound. The parameters of the reflected particle at the rebound instant are determined by a semi-empirical model of particle-wall impact interaction [10], which yields the following relations for the normal-to-wall and tangential-to-wall components of the velocity vector of the center of mass of the particle v_{pn}^+ and $v_{p\tau}^+$ and its angular velocity ω_p^+:

$$v_{pn}^+ = -a_n v_{pn}^-, \qquad v_{p\tau}^+ = \begin{cases} a_\tau v_{p\tau}^- + \omega_p^- r_p (a_\tau - 1), & \beta < \beta_*, \\ a_\tau v_{p\tau}^- - 2\omega_p^- r_p/7, & \beta \geq \beta_*, \end{cases}$$

$$\omega_p^+ = \begin{cases} 5v_{p\tau}^-(a_\tau - 1)/(2r_p) + 5\omega_p^-(a_\tau - 3/5)/2, & \beta < \beta_*, \\ -v_{p\tau}^- a_\tau / r_p + 2\omega_p^-/7, & \beta \geq \beta_*. \end{cases} \tag{7}$$

Here the particle parameters before its collision with the surface are denoted by the superscript minus; a_n and a_τ are the restitution coefficients of the normal and tangential components of the velocity vector; $0^\circ \leq \beta \leq 90^\circ$ is the angle between the velocity vector of the incident particle and the surface. The conditions $\beta < \beta_*$ and $\beta \geq \beta_*$ correspond to particle slipping along the surface under impact interaction and to the absence of particle slipping, respectively. The coefficients a_n and a_τ are calculated by the formulas [10, 11]

$$a_n = 1 - [1 - \exp(-0.1|\boldsymbol{v}_p^-|^{0.61})]\sin\beta, \qquad |\boldsymbol{v}_p^-| = [(v_{pn}^-)^2 + (v_{p\tau}^-)^2]^{1/2},$$

$$a_\tau = C_0 + C_1(\pi/2 - \beta)^2 + C_2(\pi/2 - \beta)^4 + C_3(\pi/2 - \beta)^6. \tag{8}$$

The value of the angle β_* in Eqs. (7) and the constants C_0, C_1, C_2, and C_3 in Eqs. (8) depend on the particle and wall materials and on the state of the surface [10, 11]. The following values were used for these quantities in the present work: $\beta_* = 0.1911$, $C_0 = 0.690$, $C_1 = -0.288$, $C_2 = 0.114$, and $C_3 = 0.0219$. These values correspond to solid particles, such as corundum or quartz sand, and a steel wall.

At the initial time, before diaphragm opening, the particles in the high-pressure chamber do not move and have a random equiprobable distribution.

Numerical Method. The carrier gas flow is numerically simulated by a finite-volume method. A substantially nonuniform unstructured grid is generated in the computational domain in the plane (x, y); the grid is composed of triangular elements and is substantially refined in the nozzle throat and near the model in the test section. Another grid composed of polygonal cells with their centers at the triangle vertices is constructed over the first grid. For these cells, the gas-dynamic equations (1) are written in the following integral form with the use of the Ostrogradskii–Gauss theorem:

$$\frac{\partial}{\partial t}\int\limits_{\Omega_i} \boldsymbol{U}\, d\Omega + \int\limits_{S_i} (\boldsymbol{F}\, n_x + \boldsymbol{G}\, n_y)\, dS + \int\limits_{\Omega_i} \frac{\boldsymbol{H}}{y}\, d\Omega = 0$$

[Ω_i and S_i are the cell area and boundary; $\boldsymbol{n}(n_x, n_y)$ is the outward unit normal vector to the boundary]. The integrals over Ω_i are approximated with the use of the mean-value theorem. In calculating the integral over S_i, the boundary of the polygonal cell is divided into individual faces. The flux vectors $\boldsymbol{F}\, n_x + \boldsymbol{G}\, n_y$ through each face of the cell are calculated by Godunov's method [12] with a MinMod limiter [13] suppressing oscillations of gas parameters near shock-wave fronts. A predictor–corrector scheme is used to approximate the derivative with respect to time. The numerical method is described in detail in [3].

For obtaining the flow pattern of the dispersed phase, Eqs. (2) for a large number of particles are solved simultaneously with the equations of motion of the carrier gas. A second-order predictor–corrector scheme is used:

$$\boldsymbol{v}_p^* = \boldsymbol{v}_p^n + \frac{\Delta t_p}{m_p}\,(\boldsymbol{f}_D^n + \boldsymbol{f}_{\mathrm{M}}^n), \qquad \boldsymbol{\omega}_p^* = \boldsymbol{\omega}_p^n + \frac{\Delta t_p}{J_p}\,\boldsymbol{l}_p^n, \qquad \boldsymbol{r}_p^* = \boldsymbol{r}_p^n + \Delta t_p\, \boldsymbol{v}_p^n,$$

$$\boldsymbol{v}_p^{n+1} = \boldsymbol{v}_p^n + \frac{\Delta t_p}{2m_p}\,(\boldsymbol{f}_D^n + \boldsymbol{f}_D^* + \boldsymbol{f}_{\mathrm{M}}^n + \boldsymbol{f}_{\mathrm{M}}^*), \quad \boldsymbol{\omega}_p^{n+1} = \boldsymbol{\omega}_p^n + \frac{\Delta t_p}{2J_p}\,(\boldsymbol{l}_p^n + \boldsymbol{l}_p^*), \quad \boldsymbol{r}_p^{n+1} = \boldsymbol{r}_p^n + \frac{\Delta t_p}{2}\,(\boldsymbol{v}_p^n + \boldsymbol{v}_p^*).$$

The parameters of the gas phase at a point where the particle is located are determined by bilinear interpolation of these parameters over the element of the triangular grid through which the particle flies.

The time step of integration in calculating the gas flow is determined from the Courant–Friedrichs–Lewy condition. The time step in calculating the particle trajectories is determined from the condition that the distance covered by the particle within one time step does not exceed the linear size of the triangle where the particle is located. In addition to particle trajectories, the volume fractions of particles in the nozzle and in the test section ahead of the model are calculated. In these simulations, the dispersed phase is considered as a discrete medium, and its behavior is modeled by a large number of test particles, each of them, in turn, simulating the motion of a certain cloud of real dispersed particles [14]. The total number of test particles in the computational domain is approximately $2 \cdot 10^6$.

In the numerical model, the test particles are initially located in the high-pressure chamber in a region 2 m long adjacent to the diaphragm. The position of the left boundary of the region is chosen on the basis of preliminary calculations under the condition that the quasi-steady two-phase flow around the model persists for at least 5 msec before all test particles fly through the test section. The initial positions of the test particles in an arbitrary ith polygonal cell of the computational domain in the plane (x, y) is randomly defined in accordance with the uniform distribution law. A weight coefficient is used for each test particle in the ith cell: $\nu_i = N_i/M_i$, where $N_i = \alpha_{p\infty} V_i/V_p$ is the number of real dispersed particles in a toroidal volume V_i with a cross section Ω_i, $V_p = (4/3)\pi r_p^3$ is the volume of one particle, Ω_i is the area of the ith cell, $M_i = \Omega_i M_\Sigma/\Omega_\Sigma$ is the number of test particles in the ith cell, and $M_\Sigma = \sum\limits_i M_i$ and $\Omega_\Sigma = \sum\limits_i \Omega_i$ are the total number of test particles and the total area of computational cells in the plane (x, y) where the particles are located at the initial time. The weight coefficient ν_i is the number of real particles in the cloud modeled by the ith test particle.

To calculate the volume fraction of particles α_p at a point (x_k, y_k), a rectangular cell with the center at this point is generated at the time t. Test particles located at this time instant in this cell are determined. In the toroidal volume V_k formed by the cell considered, the number of real particles $N_k = \sum\limits_j \nu_j$ is calculated (summation is performed over all test particles within the cell), and then the volume fraction $\alpha_p = V_p N_k/V_k$ is found. The cell area and, correspondingly, the volume V_k are chosen from the condition that the number of test particles in the cell should be sufficiently large for statistical stability of the quantity α_p (normally, the number of test particles is about 10^3). In the case of a quasi-steady flow of a two-phase mixture, the cell area is chosen to be rather small,

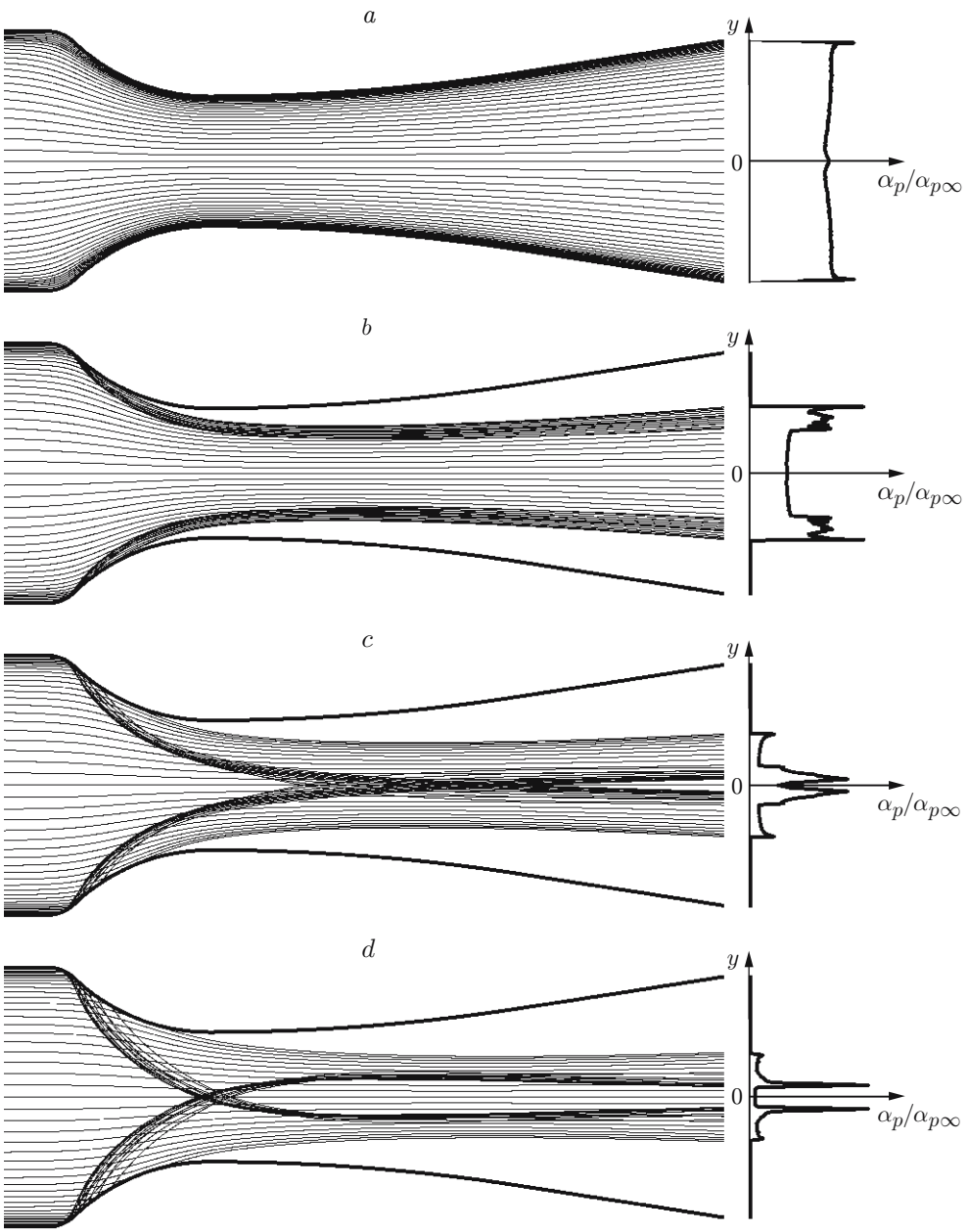

Fig. 2. Particle trajectories in the throat of the Laval nozzle (left) and profiles of dimensionless volume fraction of particles on the right boundary (right) in a quasi-steady flow regime: $d_p = 0.15$ (a), 10 (b), 20 (c), and 40 μm (d).

the number of test particles traversing the cell during the time interval Δt is calculated, and the result is averaged over Δt.

Simulation Results. The possibility of using a hypersonic shock tunnel for experimental investigations of a uniform two-phase gas–particle flow around various models is determined by three parameters: duration of the quasi-steady regime of the two-phase flow in the test section, nonuniformity of the distribution of the volume fraction of particles across the flow ahead of the model, and the time lag between the dispersed phase and the carrier gas flow. All these parameters depend on the particle behavior. Particles of different sizes have different inertia and, correspondingly, different velocity lag with respect to the gas flow, which affects both the process of stabilization of the quasi-steady flow around the model and the structure of the dispersed phase flow.

Let us consider the particle trajectories in the nozzle throat in a quasi-steady flow (Fig. 2). Particles with a diameter $d_p = 0.15$ μm occupy almost the entire flow region (Fig. 2a), and the cross-sectional distribution of

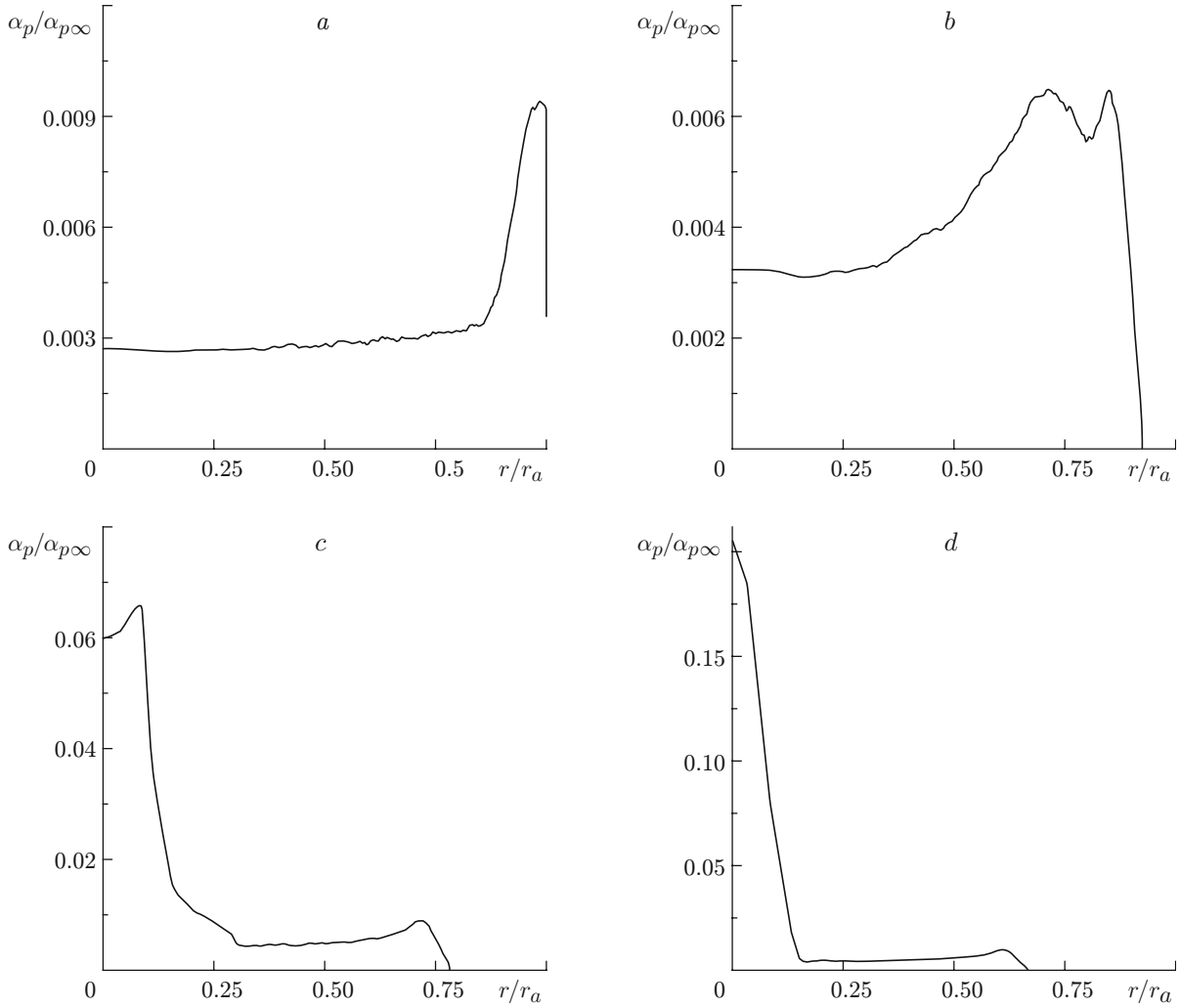

Fig. 3. Distribution of the dimensionless volume fraction of particles at the test-section entrance in a quasi-steady flow regime: $d_p = 5$ (a), 10 (b), 15 (c), and 20 μm (d).

their volume fraction is close to uniform. Actually, the particles move along the streamlines of the carrier gas. The velocity lag of these particles behind the gas flow is less than 0.1 m/sec. Larger particles ($d_p \geqslant 5$ μm) moving in the near-wall region collide with the walls of the converging part of the nozzle and become reflected from the walls. The reflected particles form thin layers in the flow, which may be non-intersecting (Fig. 2b) or intersecting (Figs. 2c and 2d). The volume fraction of particles in these layers is much higher than that in the main flow. As a result, the cross-sectional distribution of the volume fraction of particles becomes essentially nonuniform (the profiles shown in Fig. 2 on the right are plotted in different scales, because the maximum value of $\alpha_p/\alpha_{p\infty}$ substantially depends on d_p). For $d_p = 0.15$, 10, 20, and 40 μm, we have $(\alpha_p/\alpha_{p\infty})_{\max} = 0.15$, 0.8, 5.0, and 11.0, respectively. This nonuniformity persists in the test section (Fig. 3). It follows from Fig. 3 that an increase in particle diameter from 10 to 15 μm induces qualitative changes in the profiles (r_a is the nozzle-exit radius).

In formulating the mathematical model of a two-phase flow, the influence of the dispersed phase on the carrier gas was ignored. The validity of this assumption, however, becomes doubtful as thin layers with high concentrations of particles appear. The envelope surface of the trajectories of particles reflected from the walls is a caustics with the volume fraction of particles formally tending to infinity. As was shown in [15], though the volume fraction of particles on the caustics proper becomes infinite, the mean volume fraction of particles in an arbitrary vicinity of the caustics of this type is finite. Actually, this means that the mean volume fraction of particles in each cell of the grid used to solve the carrier gas equations numerically is (even formally) a finite quantity. For an extremely fine

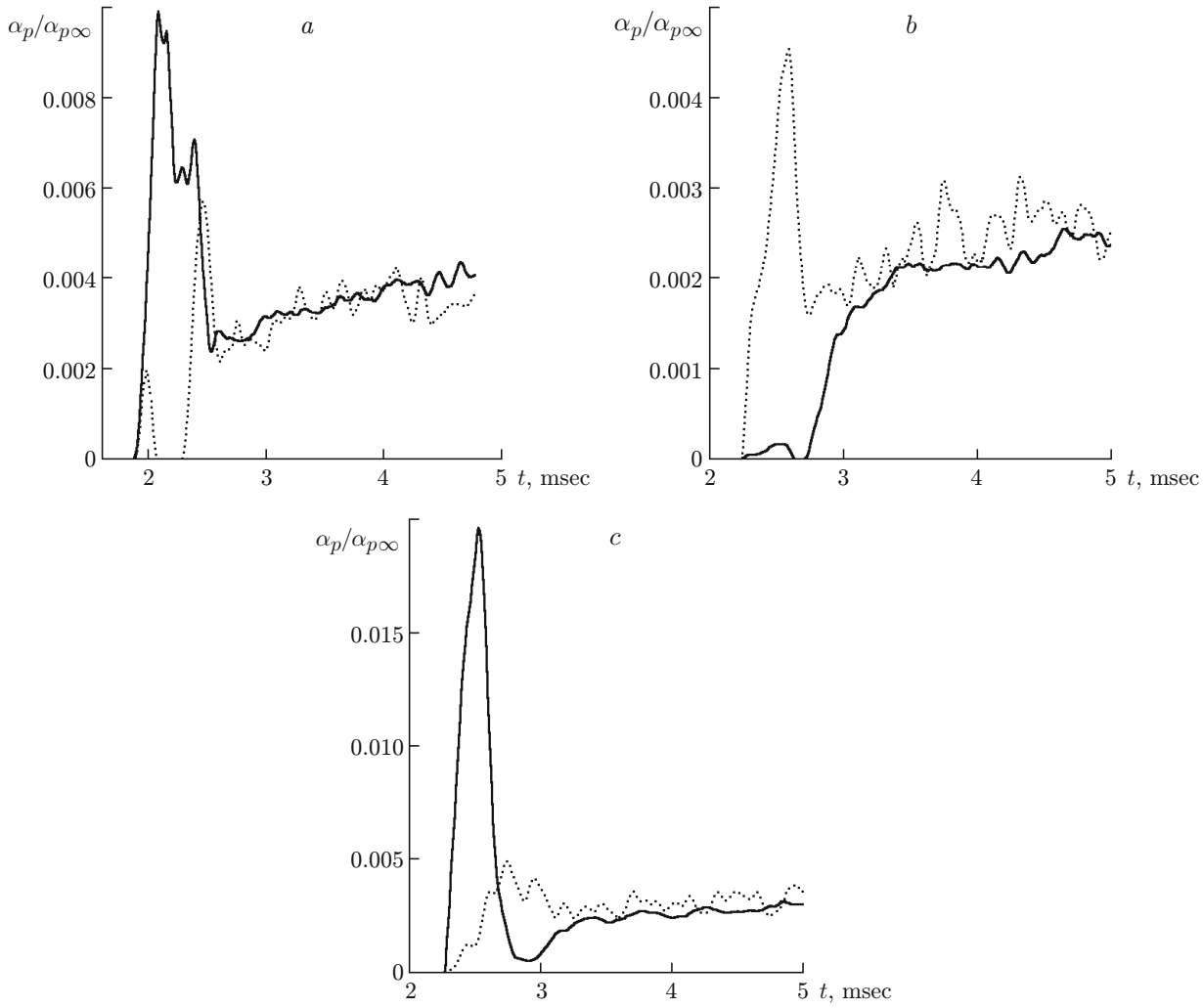

Fig. 4. Time evolution of the dimensionless volume fraction of particles of different sizes in the test section ahead of the model on the axis (solid curves) and at a distance of 41 mm from the axis (dashed curves): $d_p = 0.15$ (a), 5 (b), and 10 μm (c).

grid used in the present simulations (more than 300,000 cells), the highest volume fraction of particles α_p in cells located inside the layers with high volume fractions of the dispersed phase is obtained for the coarsest particles with a diameter $d_p = 40$ μm, and even in this case it does not exceed $\alpha_p = 2 \cdot 10^{-6}$. Based on the estimates obtained in [4], we can easily show that the effect of the dispersed phase with such a low concentration on the carrier gas is extremely small and can be neglected.

The carrier gas flow in the test section has a velocity of 1051 m/sec. Particles always fall behind the gas flow, and the lag depends on the particle size. Thus, the velocity of particles with diameters $d_p = 1$, 5, 10, 20, and 40 μm is smaller than the gas flow velocity by 1, 22, 77, 162, and 250 m/sec, respectively.

A quasi-steady two-phase flow in the nozzle and near the model in the test section is stabilized after some transitional processes. The initial stage of these processes was studied in [3], where the leading front of particles of all sizes moving in the nozzle toward the test section was demonstrated to have a complicated (nonflat) shape. The distributions of the dispersed phase behind the front, both along and across the flow, are extremely nonuniform, and the streamwise length of this region can be several diameters of the nozzle exit. After interaction of this region with the model, the latter finally experiences the action of a quasi-steady two-phase flow.

Figure 4 shows the time evolution of the dimensionless volume fraction of particles in the test section ahead of the model on the axis and at a distance of 41 mm from the axis (the distance at which the models were located in some series of physical experiments [2]). The oscillations in the graphs are, apparently, caused by the scatter (dispersion)

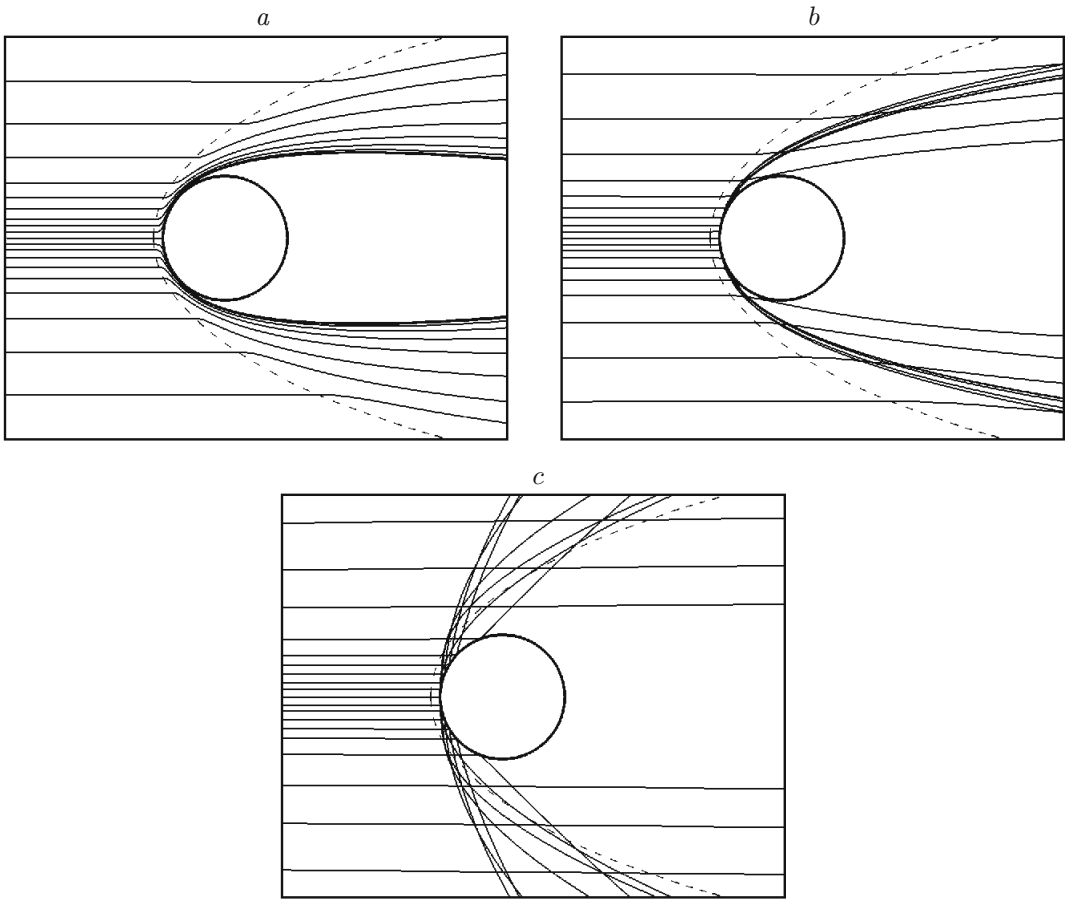

Fig. 5. Trajectories of particles of different fractions near the model (sphere) in the test section in a quasi-steady flow regime: $d_p = 0.15$ (a), 1 (b), and 15 μm (c); the dashed curve indicates the bow shock wave.

of the volume fractions of particles with the number of test particles used in simulations (approximately $2 \cdot 10^6$). For comparison, we should note that approximately 10^6 particles should be located in the shock layer ahead of the model to obtain the field of the volume fraction of particles in this layer without oscillations [16]. It follows from Fig. 4 that the quasi-steady flow of the dispersed phase in the test section is reached approximately in 2 msec after the particle front has passed. Note that the quasi-steady carrier gas flow around the model is reached approximately in 4.8 msec after shock-tunnel start-up. For extremely fine particles ($d_p = 0.15$–1.00 μm), the regime of the quasi-steady two-phase flow around the model is reached almost simultaneously with the quasi-steady flow of the carrier gas, while the quasi-steady regime for coarse particles is reached much later because of the velocity lag of the dispersed phase. Thus, for particles 20 μm in diameter, the quasi-steady regime of the particle flow is reached approximately in 1 msec after stabilization of the gas flow. The estimates show that the duration of the quasi-steady gas flow near the model is 12 msec. Based on the above-given considerations, the delay in stabilization of the two-phase flow regime, as compared with stabilization of the pure gas regime, can be regarded as insignificant even for the coarsest particles considered.

Figure 5 shows the trajectories of particles of different sizes near the model in the quasi-steady flow regime. The flow structures are substantially different for fine particles ($d_p = 0.15$ μm) and for coarser particles. The finest particles fly around the model without colliding with the model surface. Particles 1 μm in diameter collide with the model and rebound from the model surface, but they stay within the region behind the bow shock wave. Coarser particles ($d_p \gtrsim 5$ μm) become reflected from the model surface and leave the shock layer. The motion of reflected particles is accompanied by numerous intersections of trajectories, which makes the particle flow structure much more complicated.

This work was supported by the Russian Foundation for Basic Research (Grant No. 05-08-50075).

REFERENCES

1. *Shock Tunnels* (collected scientific papers) [translation into Russian], Izd. Inostr. Lit., Moscow (1962).
2. É. B. Vasilevskii, A. N. Osiptsov, A. V. Chirikhin, and L. V. Yakovleva, "Heat transfer on the frontal surface of a blunt body in a high-velocity flow containing low-inertia particles," *Inzh.-Fiz. Zh.*, **74**, No. 6, 29–37 (2001).
3. A. Verevkin and Yu. Tsirkunov, "Numerical investigation of two-phase gas-particle flow in a hypersonic shock tunnel," in: *Proc. of the Europ. Conf. on Comput. Fluid Dynamics*, Egmond aan Zee (The Netherlands) (2006); CD-ROM: Proc. ECCOMAS CFD (2006), Paper No. 211.
4. Yu. M. Tsirkunov, "Gas-particle flows around bodies — key problems, modeling and numerical analysis," in: *Proc. of the 4th Int. Conf. on Multiphase Flow*, New Orleans (2001), CD-ROM: Proc. ICMF'2001 (2001), Paper No. 607.
5. Ch. B. Henderson, "Drag coefficients of spheres in continuum and rarefied flows," *AIAA J.*, **14**, No. 6, 707–708 (1976).
6. N. N. Yanenko, R. I. Soloukhin, A. N. Papyrin, and V. M. Fomin, *Supersonic Two-Phase Flows under Conditions of Velocity Nonequilibrium of Particles* [in Russian], Nauka, Novosibirsk (1980).
7. S. I. Rubinow and J. B. Keller, "The transverse force on a spinning sphere moving in a viscous fluid," *J. Fluid Mech.*, **11**, 447–459 (1961).
8. B. Oesterlé and T. Bui Dinh, "Experiments on the lift of a spinning sphere in a range of intermediate Reynolds numbers," *Exp. Fluids*, **25**, 16–22 (1998).
9. S. C. R. Dennis, S. N. Singh, and D. B. Ingham, "The steady flow due to a rotating sphere at low and moderate Reynolds numbers," *J. Fluid Mech.*, **101**, 257–279 (1980).
10. Yu. M. Tsirkunov, S. V. Panfilov, and M. B. Klychnikov, "Semi-empirical model of impact interaction of a dispersed particle with the surface in a gas-suspension flow," *Inzh.-Fiz. Zh.*, **67**, Nos. 5/6, 379–386 (1994).
11. V. A. Lashkov, "Experimental determination of the coefficients of restitution of particles in the flow of a gas suspension in a collision against the surface," *J. Eng. Phys. Thermophys.*, **60**, No. 2, 154–159 (1991).
12. S. K. Godunov, A. V. Zabrodin, M. Ya. Ivanov, et al., *Numerical Solution of Multidimensional Problems of Gas Dynamics* [in Russian], Nauka, Moscow (1976).
13. A. G. Kulikovskii, N. V. Pogorelov, and A. Yu. Semenov, *Mathematical Aspects of the Numerical Solution of Hyperbolic Systems of Equations* [in Russian], Fizmatlit, Moscow (2001).
14. C. T. Crowe, "Review: Numerical models for dilute gas-particle flows," *Trans. ASME, Ser. I: J. Fluids Eng.*, **104**, 297–303 (1982).
15. A. N. Osiptsov, "Investigation of zones of unlimited growth of particle concentration in dispersed flows," *Izv. Akad. Nauk SSSR, Mekh. Zhidk. Gaza*, No. 3, 46–52 (1984).
16. A. N. Volkov and Yu. M. Tsirkunov, "Effect of the dispersed phase on the flow and heat transfer in a supersonic dusty-gas flow around a transverse cylinder," *Izv. Ross. Akad. Nauk, Mekh. Zhidk. Gaza*, No. 4, 67–83 (2005).